

# Spin dynamics and an orbital-antiphase pairing symmetry in iron-based superconductors

Z. P. Yin,\* K. Haule, and G. Kotliar

*Department of Physics and Astronomy, Rutgers University, Piscataway, NJ 08854, United States.*

(Dated: November 1, 2013)

The symmetry of the wave function describing the Cooper pairs is one of the most fundamental quantities in a superconductor but its measurement in the iron-based superconductors has proved to be very difficult. The complex multi-band nature of these materials makes the interplay of superconductivity with spin and orbital dynamics very intriguing, leading to very material dependent magnetic excitations, and pairing symmetries.<sup>1-3</sup> Here we use first-principles many-body method, including *ab initio* determined two-particle vertex function, to study the spin dynamics and superconducting pairing symmetry in a large number of iron-based superconductors. In iron compounds with high transition temperature, we find both the dispersive high-energy spin excitations, and very strong low energy commensurate or nearly commensurate spin response, suggesting that these low energy spin excitations play the dominate role in cooper pairing. We find three closely competing types of pairing symmetries, which take a very simple form in the space of active iron  $3d$  orbitals, and differ only in the relative quantum mechanical phase of the  $xz$ ,  $yz$  and  $xy$  orbital contributions. The extensively discussed  $s^{+-}$  symmetry appears when contributions from all orbitals have equal sign, while the opposite sign in  $xz$  and  $yz$  orbitals leads to the  $d$  wave symmetry. A novel orbital antiphase  $s^{+-}$  symmetry emerges when  $xy$  orbital has opposite sign to  $xz$  and  $yz$  orbitals. We propose that this orbital-antiphase pairing symmetry explains the puzzling variation of the experimentally observed superconducting gaps on all the Fermi surfaces of LiFeAs<sup>4,5</sup>. This novel symmetry of the order parameter may be realized in other iron superconductors.

The spin and the multi-orbital dynamics of iron based superconductors is believed the play the essential role in the mechanism of superconductivity<sup>6</sup>, but a realistic modeling of magnetic excitations, and a clear physical picture for their variation across different families of iron superconductors, is currently lacking. The Cooper pairs are locked into singlets but the orbital structure of the superconducting order parameter can be material dependent, and its connection to orbital and spin excitations is an open problem. To address these issues, we use *ab initio* theoretical method for correlated electron materials, based on combination of dynamical mean field theory (DMFT) and density functional theory (DFT)<sup>7</sup>. This computational method improves on DFT description of electronic structure in iron superconductors, and predicts correct magnitude of ordered magnetic moments<sup>8</sup>, improves electronic spectral function and Fermi surfaces<sup>8,9</sup>, and charge response such as optical conductivity<sup>10</sup>. To successfully predict dynamical magnetic response across different families of iron superconductors, and superconducting pairing, it is crucial to compute from *ab initio* the two particle scattering amplitude also called the two particle vertex function.<sup>11</sup> Its complex calculation previously precluded *ab initio* description of trends across different families of iron superconductors, as spin response is very sensitive to the value and the energy dependence of this screened interaction. In many methods used earlier, such as random phase approximation, it is treated as a static adjustable parameter<sup>12,13</sup>, or it was computed by summing very limited subset of Feynman diagrams<sup>14</sup>. Within the functional renormalization group<sup>15</sup> this screened interaction is computed rather well, but the electronic structure is greatly simplified, treating the Hubbard model for iron  $d$ -bands only, and usually neglecting renormalization of electronic structure due to electronic correlations. Similar simplification is made in strong-coupling approaches.<sup>16</sup>

All iron-based superconductors contain similar layers of tetrahedra with iron in the center and pnictogen/chalcogen at the corners, but their spin excitation spectra varies greatly among compounds. In Fig. 1 we plot the dynamic spin structure factor  $S(q, \omega) = \chi''(q, \omega) / (1 - \exp(-\hbar\omega/k_B T))$  for several classes of iron compounds along the high symmetry momentum path in the first Brillouin zone of the single iron unit cell. We overlay the neutron scattering data<sup>17-20</sup> for some compounds where experiment is available, to show a good agreement between theory and experiment. The spin-wave bandwidth, defined as the difference between the minimum ( $q = (1, 0)$ ) and the maximum ( $q = (1, 1)$ ) of spin excitation is related to spin-exchange  $J$ , which is inversely proportional to the strength of the low energy Coulomb interaction ( $J \propto t^2/U$ ), hence increased correlation strength leads to smaller bandwidth. Notice that the correlation strength in these compounds is dominated by the Fe-pnictogen distance, as shown in Ref. 8. The phosphorus compounds (Figs. 1a-c) show the largest spin wave bandwidth of the order of 0.6 eV-0.45 eV, which is a consequence of their most itinerant nature among these compounds<sup>8</sup>. The mass enhancement due to correlations is increased in arsenides and even more in chalcogenides<sup>8</sup>, hence the spin-wave bandwidth is progressively reduced to 0.3 – 0.2 eV in Figs. 1d-f, and 0.15 eV in Figs. 1g-h. The intensity of spin excitation is proportional to the size of the fluctuating moment in this energy range, which roughly anti-correlates with strength of correlations, hence phosphorus compounds

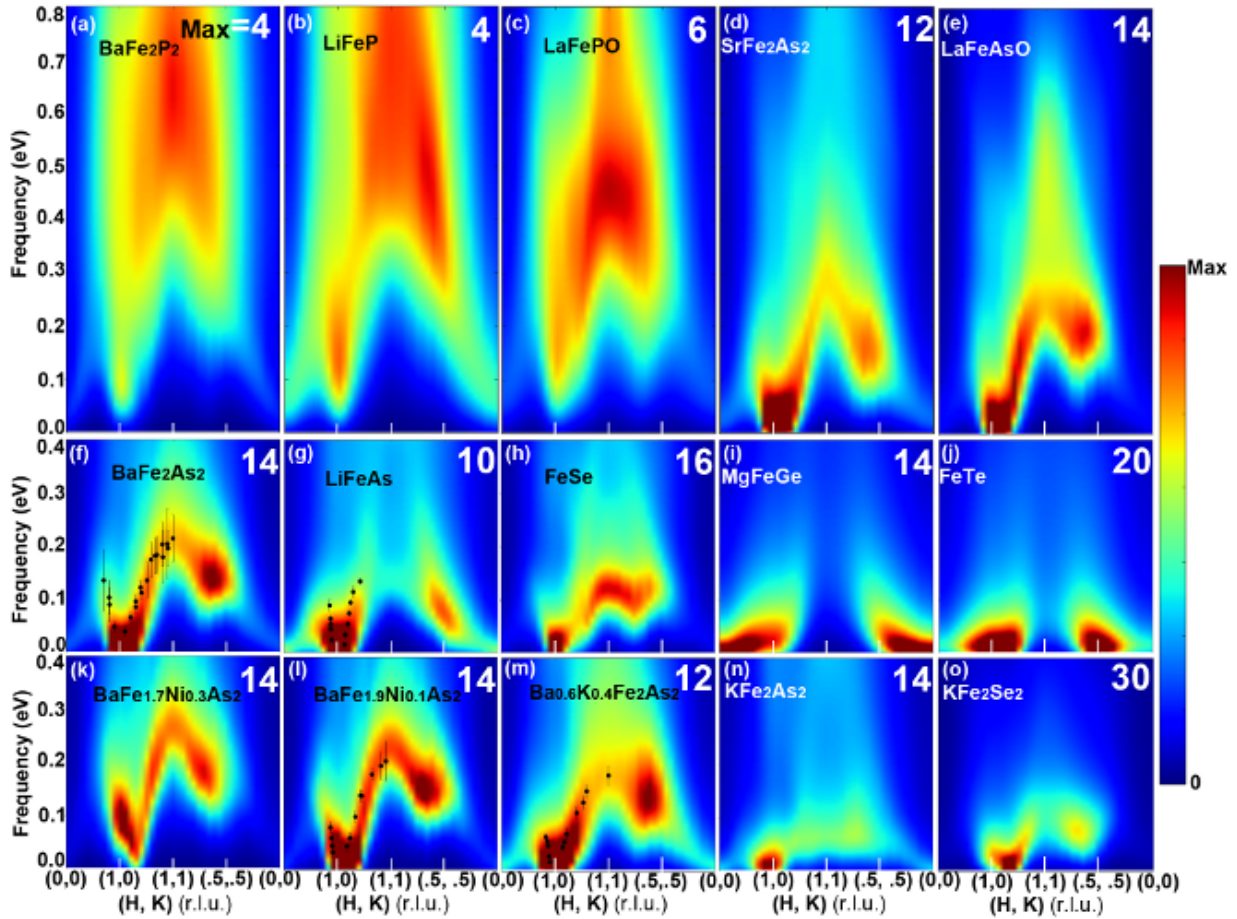


FIG. 1: Dynamic spin structure factor  $S(q, \omega)$  in iron pnictides, chalcogenides and MgFeGe. The  $S(q, \omega)$  is plotted along the high-symmetry path  $(H, K, L = 1)$  in the first Brillouin zone of the single iron unit cell. The intensity varies substantially across these compounds, hence the maximum value of the intensity was adjusted to emphasize the dispersion most clearly. The maximum value of the intensity in each compound is shown in the top right corner. The color coding corresponds to the theoretical calculations for (a) BaFe<sub>2</sub>P<sub>2</sub> ( $T_C^{max} < 2K$ ); (b) LiFeP ( $T_C = 6K$ ); (c) LaFePO ( $T_C = 7K$ ); (d) SrFe<sub>2</sub>As<sub>2</sub> ( $T_C^{max} = 37K$ ); (e) LaFeAsO ( $T_C^{max} = 43K$ ); (f) BaFe<sub>2</sub>As<sub>2</sub> ( $T_C^{max} = 39K$ ); (g) LiFeAs ( $T_C = 18K$ ); (h) FeSe ( $T_C^{max} = 37K$ ); (i) MgFeGe ( $T_C^{max} = 0$ ); (j) FeTe ( $T_C^{max} = 0$ ); (k) BaFe<sub>1.7</sub>Ni<sub>0.3</sub>As<sub>2</sub> ( $T_C < 2K$ ); (l) BaFe<sub>1.9</sub>Ni<sub>0.1</sub>As<sub>2</sub> ( $T_C = 20K$ ); (m) Ba<sub>0.6</sub>K<sub>0.4</sub>Fe<sub>2</sub>As<sub>2</sub> ( $T_C = 39K$ ); (n) KFe<sub>2</sub>As<sub>2</sub> ( $T_C = 3.5K$ ); (o) KFe<sub>2</sub>Se<sub>2</sub>. The experimental data are shown as black dots with error bars in (f), (g), (l) and (m), digitized from Refs. 17–20.

show the weakest ( $Max = 4$ ) and FeTe shows the strongest ( $Max = 20$ ) intensity.

The low energy spin-excitations are much more sensitive to the details of both the band-structure and the two-particle vertex function, hence the trend across different compounds can not be guessed from either the correlation strength or from the band structure. In Fig. 2 we show  $S(q, \omega)$  for the same compounds as in Fig. 1, but we take a different cut. We keep the energy fixed at  $\omega = 5$  meV, and change momentum in the two dimensional momentum plane  $(H, K)$  (The momentum dependence in  $z$  direction is weak for most compounds). As is clear from Figs. 1a-c, and Fig. 2a-c, the low energy spin-excitations are extremely weak ( $Max \approx 1$ ) in phosphorus compounds and the spin excitations at the spin-density wave ordering vector  $(1, 0)$  is comparable to its value at the ferromagnetic ordering vector  $(0, 0)$ . In strong contrast, the low energy spin excitations are very strong in arsenides (Fig. 2d-g) and are concentrated solely at the commensurate wave vector  $(H, K) = (1, 0)$ . This is the ordering wave vector of the spin-density wave magnetic state, which is the ground state for these parent compounds, except superconducting LiFeAs ( $T_C = 18K$ ). When doped, all compounds in Figs. 2d-f are high-temperature superconductors ( $T_c \approx 37K - 39K$ ). Similarly chalcogenide FeSe (Fig. 1h), which becomes superconducting at  $T_c = 37K$  under modest pressure  $p = 3$  GPa, has similar low energy spin response as the arsenides superconductors.

On the other hand, MgFeGe is a compound with similar band structure as LiFeAs, hence the random-phase approximation gives similar spin response in the two compounds with low energy maximum intensity at  $(1, 0)$ .<sup>21</sup> Inclusion of the realistic two-particle vertex function, as done in this study, has a profound impact on the spin

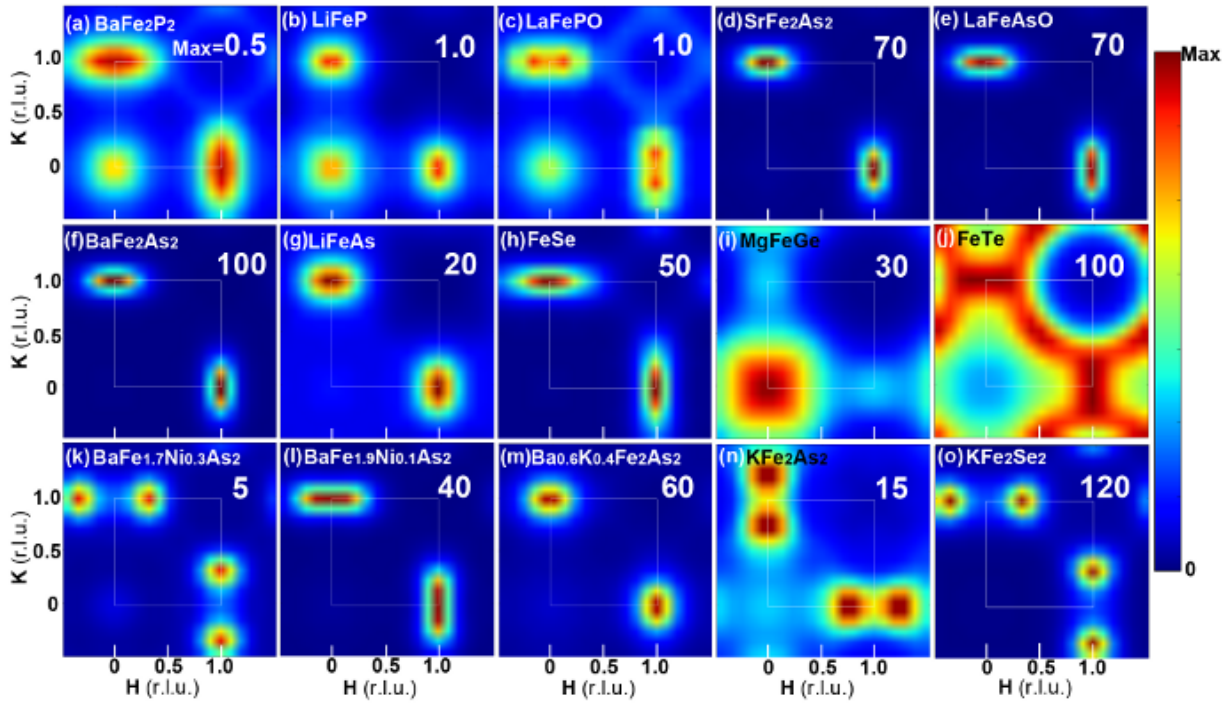


FIG. 2: **Dynamic spin structure factor  $S(q, \omega)$  in iron pnictides, chalcogenides and MgFeGe.** The  $S(q, \omega)$  is plotted in the 2D plane  $(H, K)$  at constant  $\omega=5$  meV for the same materials as in Fig.1. The maximum intensity scale for each compound is marked as a number in the top-right corner of each subplot. We take the cut at  $L = 1$  for all compounds except MgFeGe and phosphorus compounds, where  $L = 0$  plane is shown to emphasize their tendency towards ferromagnetism.

excitations. A broad maximum appears at  $(0, 0)$  (see Fig. 2i), hence spin fluctuations are ferromagnetic in agreement with calculation of Ref. 22 showing stable ferromagnetic ground state. Finally FeTe has also much broader spin-excitations covering a large part of the Brillouin zone (see Fig. 2j), and shows two competing excitations at  $q=(1,0)$  and  $q=(0.5, 0.5)$ , the latter corresponds to the ordering wave vector of the low-temperature antiferromagnetic state of  $\text{Fe}_{1.07}\text{Te}$ .<sup>23</sup>

The common theme in high-temperature superconductors (Figs. d-h) is thus the existence of well defined high energy dispersive spin excitations with bandwidth between  $0.1 - 0.35$  eV, and most importantly very well developed commensurate (or nearly commensurate) low energy spin excitations at wave vector  $q = (1, 0)$ , consistent with the theory of spin-fluctuation mediated superconductivity<sup>24,25</sup>. The pnictide parent compounds  $\text{SrFe}_2\text{As}_2$ ,  $\text{LaFeAsO}$ ,  $\text{BaFe}_2\text{As}_2$  have strong low energy spin excitation centered exactly at  $q = (1, 0)$ , while in  $\text{LiFeAs}$  and  $\text{FeSe}$  the spin excitation is peaked slightly away from this commensurate wave vector. Consequently, the former three compounds have antiferromagnetic ground state, while the latter two are superconducting. In the former, electron or hole doping is needed to suppress the long range magnetic order, and to stabilize the competing superconducting state. In Figs. 1f,k-n and Figs. 2f,k-n we illustrate the doping dependence of the spin-excitation spectrum on the examples of electron doped and hole doped  $\text{BaFe}_2\text{As}_2$ , i.e.,  $\text{BaFe}_{1-x}\text{Ni}_x\text{As}_2$  and  $\text{Ba}_{1-x}\text{K}_x\text{Fe}_2\text{As}_2$ , respectively. The electron doping slightly increases the bandwidth (comparing Fig. 1(f) with Fig. 1(k)), whereas the hole doping dramatically reduces the bandwidth from  $\sim 0.2$  eV to  $\sim 0.05$  eV in overdoped  $\text{KFe}_2\text{As}_2$ <sup>20,26</sup> (Fig. 1(n)). The low energy spin excitations in the electron overdoped  $\text{BaFe}_{1.7}\text{Ni}_{0.3}\text{As}_2$  become very weak and strongly incommensurate<sup>20</sup> with peak centered at  $q=(1.0, 0.35)$  (see Fig. 2k). Similarly, on the hole overdoped side in  $\text{KFe}_2\text{As}_2$ , the low-energy spectrum is suppressed (maximum intensity in Fig. 2n is 15 compared to 100 in the parent compound), and main excitation peak moves to incommensurate  $q=(0.75, 0)$  in agreement with experiment.<sup>20,27</sup> The optimally doped compounds (Figs. 1l,m) have high energy spin excitations very similar to the parent compound, while the low energy excitations are slightly reduced and broadened in momentum space (Fig. 2l,m), to suppress long range magnetic order of the parent compound. This is very similar to the spectrum of  $\text{LiFeAs}$  and  $\text{FeSe}$ , which both have superconducting ground state. From these plots, we can deduce that near commensurate or commensurate spin excitations at  $q = (1, 0)$ , with some finite width in momentum space to reduce the tendency towards the long-range order, are favorable for superconductivity.

Now we comment on the complexity of the  $\text{K}_x\text{Fe}_{2-y}\text{Se}_2$  compounds. Our results for  $\text{KFe}_2\text{Se}_2$  in Figs. 1&2(o) indicate strong low energy spin excitation peaked around  $q = (1, 0.4)$ . Vacancies in the K site, which reduce the

effective electron doping, can move the peak towards  $q = (1, 0)$  and favor superconductivity. On the other hand, vacancies in the Fe sites can move the peak to  $q=(0.6, 0.2)$  to induce novel magnetism in  $\text{K}_{0.8}\text{Fe}_{1.6}\text{Se}_2$ <sup>28</sup>.

Whereas the dynamic spin structure factor  $S(q, \omega)$  dispersion and the strength of the low energy spin excitations correlate with experimental  $T_c$  across many families of iron superconductors, the superconducting pairing symmetry and the variation of the superconducting gaps on the different Fermi surfaces cannot be extracted from the spin dynamics alone. To make further progress on these issues, we computed the complete two particle scattering amplitude in the particle-particle channel within the dynamical mean field theory framework, and we solved Eliashberg equations in the BCS low energy approximation (see Supplementary material). In the Eliashberg equations, the orbital degrees of freedom play the central role, rather than the bands, because the Coulomb interaction, and the two particle irreducible vertex function in the particle-hole channel, is large between the iron-3d electrons on the same iron site.

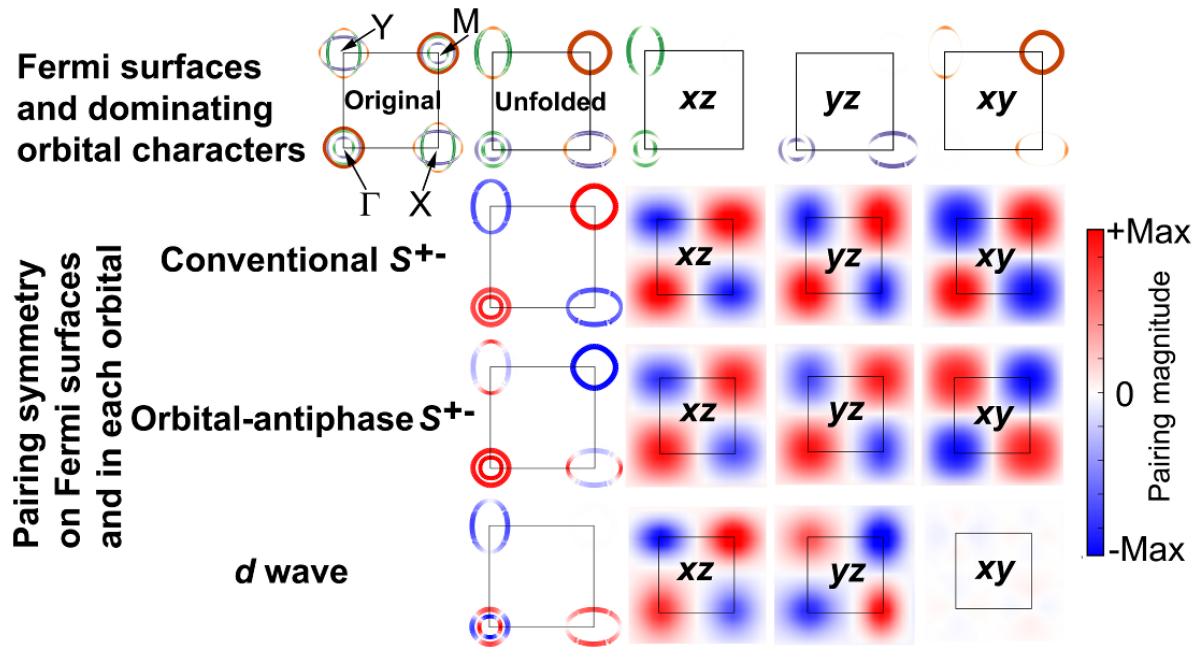


FIG. 3: **Fermi surfaces, pairing symmetries and the basic building blocks.** Top row: the original and unfolded two-dimensional Fermi surfaces in the  $\Gamma$  plane for the representative compound  $\text{LaFeAsO}$  in paramagnetic state, shown in the first Brillouin zone of the single iron unit cell. On the top right, the Fermi surfaces are further decomposed into the dominating  $\text{Fe-}t_{2g}$  ( $xz$ ,  $yz$ , and  $xy$ ) characters. The next three rows, from top to bottom, show respectively the conventional  $s^{+-}$ , the orbital-antiphase  $s^{+-}$  and the  $d$ -wave pairing symmetries of the superconducting order parameter. The left column shows the Fermi surfaces colored with strength of the order parameter  $\Delta_j(k) = \langle c_{k\uparrow,j}^+ c_{-k\downarrow,j}^+ \rangle$  ( $j$  is the band index), while the right columns decompose the order parameter in orbital space, i.e.,  $\Delta_\alpha(k) = \langle c_{k\uparrow,\alpha}^+ c_{-k\downarrow,\alpha}^+ \rangle$  ( $\alpha$  runs over  $\text{Fe-}t_{2g}$  orbitals:  $xz$ ,  $yz$ , and  $xy$ ).

In all arsenide and chalcogenide compounds with strong (nearly) commensurate low energy spin excitation, we find that the Eliashberg equations give three almost degenerate solutions with the largest eigenvalues. The corresponding three eigenvectors, which are proportional to the superconducting order parameter  $\Delta_{\alpha,\alpha'}(k)$ , are almost diagonal in orbital space ( $\alpha\alpha'$ ), and we denote the diagonal terms as  $\Delta_\alpha(k) = \Delta_{\alpha,\alpha}(k)$ . As shown in Fig. 3, these three states are similar in nature, since each orbital has sign-changing  $s^{+-}$  structure in momentum space, described by the formula

$$\Delta_\alpha(kx, ky) = \Delta_{nnn,\alpha} \cos(kx) \cos(ky) + \Delta_{nn,\alpha} (\cos(kx) + \cos(ky))/2 \quad (1)$$

but the phases on different orbitals are different. Here  $\Delta_{nn}$  correspond to the nearest-neighbor and  $\Delta_{nnn}$  to the next-nearest neighbor pairing, and we find that  $|\Delta_{nn,\alpha}| \ll |\Delta_{nnn,\alpha}|$ , hence we have predominantly next-nearest neighbor pairing. In Fig. 3 we plot Fermi surfaces and gap function in the first Brillouin zone of the single iron unit cell. We plot gap function for  $t_{2g}$  orbitals only, because gaps on the  $e_g$  orbitals are much smaller and their weight at the Fermi level is also small. Although the symmetry of pairing expressed in orbital space is  $s^{+-}$  in all three states, the projection to the Fermi surface leads to different global symmetries. When all three  $t_{2g}$  orbitals have the same phase, we recover the conventional  $s^{+-}$  state<sup>6</sup>. If the  $xz$  orbital has the opposite phase to the  $yz$  orbital, the global symmetry is of  $d$ -wave type. In this case the  $xy$  orbital shows negligible pairing. Finally, we find a novel type of

state in which  $xz$  and  $yz$  orbitals are in-phase, but the  $xy$  orbital has the opposite phase. We call this state the *orbital-antiphase  $s^{+-}$  state*.

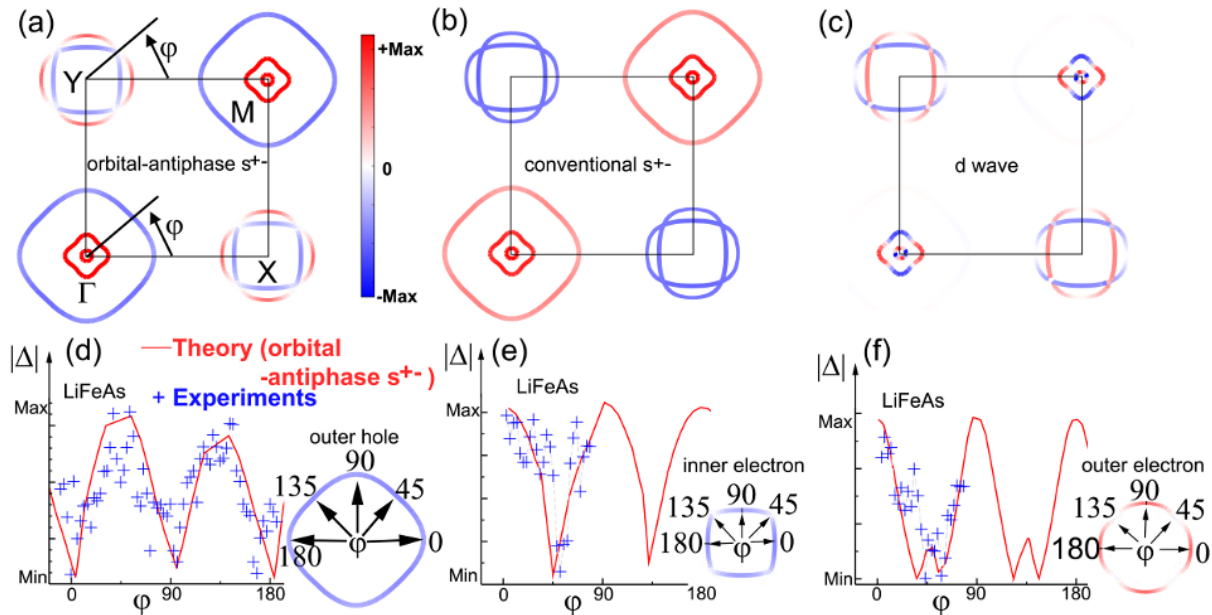


FIG. 4: **Superconducting pairing symmetry and pairing amplitude anisotropy in LiFeAs.** The superconducting order parameter  $\Delta_j(k) = \langle c_{k\uparrow,j}^+ c_{-k\downarrow,j}^+ \rangle$  on the Fermi surface, with the (a) orbital-antiphase  $s^{+-}$ , (b) conventional  $s^{+-}$  and (c) a d-wave symmetry. (d)-(f) show the variation of the pairing amplitude for the orbital-antiphase  $s^{+-}$  state on the outer hole Fermi surface and the two electron Fermi surfaces, respectively. The red lines correspond to theoretical results, and the + symbols denote the experimental measurements from Ref.4.

The identification of these basic building blocks greatly simplifies our understanding of the superconducting pairing symmetry in the iron-based superconductors, and explains why the superconducting pairing symmetry is so sensitive to the details of the electronic structure. Since flipping the sign of the order parameter in a single orbital has only a tiny energy cost, the first three eigenstates discussed above are very close in energy and have very similar eigenvalues, i.e., superconducting pairing strength. In Fig. 4 we show detailed results for LiFeAs, and we plot all the three leading pairing symmetries on the two-dimensional Fermi surfaces in the  $\Gamma$  plane of the tetragonal crystallographic unit cell. Our calculations show that the orbital-antiphase  $s^{+-}$  has the largest pairing strength in LiFeAs. Experimentally, it was found<sup>4,5</sup> that the superconducting gaps have very unusual variations on the Fermi surfaces, where the superconducting gap is maximal (minimum) around  $\phi=45^\circ$  ( $0^\circ$ ) on the outer hole Fermi surface (see Fig. 4(d)), whereas it is maximal (minimum) around  $\phi=0^\circ$  ( $45^\circ$ ) on the two electron Fermi surfaces (Fig.4(e),(f)). This observation was used as an evidence against the spin fluctuation mechanism<sup>4</sup> of superconductivity, as it is not consistent with the conventional  $s^{+-}$  state. Indeed, our calculation show that conventional  $s^{+-}$  order parameter can not account for the gap size variation in momentum space, however, as seen from (Fig.4(d)-(f)), the orbital-antiphase  $s^{+-}$  can account for the variation of this gap.

The novel orbital-antiphase  $s^{+-}$  pairing symmetry is not limited to LiFeAs but may be the pairing symmetry in many other iron-based superconductors, such as  $\text{Ba}_{1-x}\text{K}_x\text{Fe}_2\text{As}_2$  and  $\text{K}_x\text{Fe}_2\text{Se}_2$  [29]. Our study suggests that it is important to describe the cooper-pairing in orbital-space, keeping the complexity of orbital and spin fluctuations, which arise due to electron correlations, rather than solving BCS equations for weakly correlated systems in band space.

**Acknowledgments:** We thank H. Park, P. Dai and H. Ding for stimulating discussion. This work is supported by NSF DMR-1308141 (Z.P.Y. and G.K.) and NSF Career DMR-0746395 (K.H.).

\* Electronic address: yinzping@physics.rutgers.edu

<sup>1</sup> Stewart, G. R. Superconductivity in iron compounds. *Rev. Mod. Phys.* **83**, 1589-1652 (2011).

- <sup>2</sup> Hirschfeld, P.J., Korshunov, M.M., & Mazin, I.I. Gap symmetry and structure of Fe-based superconductors. *Rep. Prog. Phys.* **74**, 124508 (2011).
- <sup>3</sup> Dai, P., Hu, J., & Dagotto, E. Magnetism and its microscopic origin in iron-based high-temperature superconductors. *Nature Physics* **8**, 709-718 (2012).
- <sup>4</sup> Borisenko, S. V. *et al.* One-Sign Order Parameter in Iron Based Superconductor. *Symmetry* **4**, 251-264 (2012).
- <sup>5</sup> Umezawa, K. *et al.* Unconventional Anisotropic s-Wave Superconducting Gaps of the LiFeAs Iron-Pnictide Superconductor. *Phys. Rev. Lett.* **108**, 037002 (2012).
- <sup>6</sup> Mazin, I.I., Singh, D.J., Johannes, M.D., & Du, M. H. Unconventional Superconductivity with a Sign Reversal in the Order Parameter of  $\text{LaFeAsO}_{1-x}\text{F}_x$ . *Phys. Rev. Lett.* **101**, 057003 (2008).
- <sup>7</sup> Kotliar, G. *et al.* Electronic structure calculations with dynamical mean-field theory. *Rev. Mod. Phys.* **78**, 865-951 (2006).
- <sup>8</sup> Yin, Z.P., Haule, K., & Kotliar, G. Kinetic frustration and the nature of the magnetic and paramagnetic states in iron pnictides and iron chalcogenides. *Nature Materials* **10**, 932-935 (2011).
- <sup>9</sup> Yin, Z.P., Haule, K., & Kotliar, G. Fractional power-law behavior and its origin in iron-chalcogenide and ruthenate superconductors: Insights from first-principles calculations. *Phys. Rev. B* **86**, 195141 (2012).
- <sup>10</sup> Yin, Z.P., Haule, K., & Kotliar, G. Magnetism and Charge Dynamics in Iron Pnictides. *Nature Physics* **7**, 294-297 (2011).
- <sup>11</sup> Park, H., Haule, K., & Kotliar, G. Magnetic Excitation Spectra in  $\text{BaFe}_2\text{As}_2$ : A Two-Particle Approach within a Combination of the Density Functional Theory and the Dynamical Mean-Field Theory Method. *Phys. Rev. Lett.* **107**, 137007 (2011).
- <sup>12</sup> Kuroki, K. *et al.* Unconventional Pairing Originating from the Disconnected Fermi Surfaces of Superconducting  $\text{LaFeAsO}_{1-x}\text{F}_x$ . *Phys. Rev. Lett.* **101**, 087004 (2008).
- <sup>13</sup> Kreisel, A. *et al.* Spin fluctuations and superconductivity in  $\text{K}_x\text{Fe}_{2-y}\text{Se}_2$ . *Phys. Rev. B* **88**, 094522 (2013).
- <sup>14</sup> Onari, S. *et al.* S-wave superconductivity due to orbital and spin fluctuations in Fe-pnictides: self-consistent vertex correction with self-energy (SC-VC $\Sigma$ ) analysis. arXiv:1307.6119.
- <sup>15</sup> Wang, F., Zhai, H., Ran, Y., Vishwanath, A., & Lee, D.-H. Functional Renormalization-Group Study of the Pairing Symmetry and Pairing Mechanism of the FeAs-Based High-Temperature Superconductor. *Phys. Rev. Lett.* **102**, 047005 (2009).
- <sup>16</sup> Yu, R., Zhu, J.-X., & Si, Q. Orbital-selective superconductivity, gap anisotropy and spin resonance excitations in a multiorbital t-J1-J2 model for iron pnictides. arXiv:1306.4184.
- <sup>17</sup> Harriger, L.W. *et al.* Nematic spin fluid in the tetragonal phase of  $\text{BaFe}_2\text{As}_2$ . *Phys. Rev. B* **84**, 054544 (2011).
- <sup>18</sup> Wang, M. *et al.* Antiferromagnetic spin excitations in single crystals of nonsuperconducting  $\text{Li}_{1-x}\text{FeAs}$ . *Phys. Rev. B* **83**, 220515(R) (2011).
- <sup>19</sup> Liu, M.S. *et al.* Nature of magnetic excitations in superconducting  $\text{BaFe}_{1.9}\text{Ni}_{0.1}\text{As}_2$ . *Nature Physics* **8**, 376-381 (2012).
- <sup>20</sup> Wang, M. *et al.* A magnetic origin for high temperature superconductivity in iron pnictides. arXiv:1303.7339.
- <sup>21</sup> Rhee, H.B. & Pickett, W.E. Contrast of LiFeAs with isostructural, isoelectronic, and non-superconducting MgFeGe. *J. Phys. Soc. Jpn.* **82**, 034714 (2013).
- <sup>22</sup> Jeschke, H.O., Mazin, I.I., & Valenti, R. Why MgFeGe is not a superconductor. arXiv:1305.7368.
- <sup>23</sup> Bao, W. *et al.* Incommensurate magnetic order in the  $\alpha$ -Fe(Te,Se) superconductor systems. *Phys. Rev. Lett.* **102**, 247001 (2009).
- <sup>24</sup> Moriya, T., Takahashi, Y., & Ueda, K. Antiferromagnetic spin fluctuations and superconductivity in two-dimensional metals—a possible model for high Tc oxides. *J. Phys. Soc. Jpn.* **59**, 2905-2915 (1990).
- <sup>25</sup> Monthoux, P., Balatsky, A. V., & Pines, D. Toward a theory of high temperature superconductivity in the antiferromagnetically correlated cuprate oxide. *Phys. Rev. Lett.* **67**, 3448-3452 (1991).
- <sup>26</sup> In Ref.8, the nominal valence of Fe, as needed for double counting correction, was fixed to  $3d^6$  across all Fe compounds. To improve agreement with experiment, it is better to use the nominal valence of each compound, as has been done in the current paper, for example  $3d^{5.5}$  for Fe in  $\text{KFe}_2\text{As}_2$ . This results in a substantially larger mass enhancement (a factor of two for the  $xy$  orbital) in  $\text{KFe}_2\text{As}_2$  compared to the previous study in Ref.8.
- <sup>27</sup> Lee, C.H. *et al.* Incommensurate spin fluctuations in hole-overdoped superconductor  $\text{KFe}_2\text{As}_2$ . *Phys. Rev. Lett.* **106**, 067003 (2011).
- <sup>28</sup> Bao, W. *et al.* A Novel Large Moment Antiferromagnetic Order in  $\text{K}_{0.8}\text{Fe}_{1.6}\text{Se}_2$  Superconductor. *Chinese Phys. Lett.* **28**, 086104 (2011).
- <sup>29</sup> Ding, H. *et al.*, private communication.

## Spin dynamics and an orbital-antiphase pairing symmetry in iron-based superconductors: Supplementary information

Z. P. Yin, K. Haule, and G. Kotliar

*Department of Physics and Astronomy, Rutgers University, Piscataway, New Jersey 08854, United States.*

### I. METHOD

To carry out our first principles calculations taking into accounts strong correlation effects in the iron-based superconductors, we used a combination of density functional theory and dynamical mean field theory (DFT+DMFT) [S1] as implemented in Ref. S2, which is based on the full-potential linear augmented plane wave method implemented in Wien2K [S3], together with the full two-particle vertex correction in the same footing [S4]. The electronic charge is computed self-consistently on DFT+DMFT density matrix. The quantum impurity problem is solved by the continuous time quantum Monte Carlo method [S5,6], using Slater form of the Coulomb repulsion in its fully rotational invariant form. The local two-particle vertex is then sampled by the continuous time quantum Monte Carlo method on the fully-converged DFT+DMFT solution.

We use the same experimentally determined lattice structures as in Ref. S7, including the internal positions of the atoms (see Table S1), from References [S8–17]. We use the paramagnetic tetragonal lattice structures, and neglect the weak structural distortions. For convenience, we include the Table S1 in Ref. S7.

TABLE S1: Lattice constants and atomic positions of the compounds we studied.  $z1$  refers to the  $z$  coordinate of P/As/Se/Te and  $z2$  refers to coordinate of the other metallic atom in the 111 and 1111 structures.

Compounds	$a$ (Å)	$c$ (Å)	$z(\text{Fe})$	$z1$	$z2$	Ref.
FeTe	3.8219	6.2851	0	0.2792		S8,9
KFe <sub>2</sub> Se <sub>2</sub>	3.9136	14.0367	0.25	0.3539		S10
FeSe	3.7724	5.5217	0	0.2673		S11
LiFeAs	3.7914	6.3639	0.5	0.7365	0.1541	S12
KFe <sub>2</sub> As <sub>2</sub>	3.84	13.85	0.25	0.3531		S13
BaFe <sub>2</sub> As <sub>2</sub>	3.9625	13.0168	0.25	0.3545		S14
LaFeAsO	4.03533	8.7409	0.5	0.6512	0.14154	S15
SrFe <sub>2</sub> As <sub>2</sub>	3.9243	12.3644	0.25	0.3600		S16
LaFePO	3.96358	8.51222	0.5	0.6339	0.1487	S17
LiFeP	3.69239	6.03081	0.5	0.720055	0.151962	S18
BaFe <sub>2</sub> P <sub>2</sub>	3.84	12.44	0.25	0.3456		S19

We studied the paramagnetic phase of all compounds at the same temperature and used the same Coulomb interaction  $U$  and Hund's coupling  $J$  as in our previous work.[S7, S20, S21]

#### A. Unfolding

Since particle-hole irreducible vertices in our approach are nonzero only for electrons in the  $3d$  orbitals of the iron atoms, we can rewrite the perturbation theory in terms of vertices defined in this  $3d$  orbital subspace, and the single particle Green's function  $G_{dd}(k, \omega)$ , which starts and ends in the iron  $3d$  manifold. This Green's function can be cast into the form, where we consider only one iron per unit cell in larger Brillouin zone. This operation is usually called *unfolding*. Note that here we keep all the information from the two-iron atom calculation (for example, we have shadow bands in our Green's function), we merely rewrite perturbation theory in terms of more convenient larger Brillouin zone and one atom unit cell. We checked that for our choice of unfolding, the off-diagonal terms of the single particle Green's function in momentum  $G_{dd}(k, k + Q)$  is negligible.

To transform the electron structures from the two-iron/unit cell to the one-iron/unit cell, we used the following transformation:

$$G_{\alpha, \alpha'}(k) = \sum_{R, R'} e^{ik \cdot (R - R')} G_{R\alpha, R'\alpha'}(k) \quad (\text{S1})$$

where  $R$  and  $R'$  are the positions of the two different Fe atoms in the original crystal structure, and  $R'$  is related to  $R$  by a group symmetry operation of the crystal structure.  $\alpha, \alpha'$  labels orbitals. Special care has to be taken to the

phases of the orbitals chosen on the two iron atoms. To make off-diagonal terms in the green's function  $G_{dd}(k, k+Q)$  negligible, we need to choose different phases for the orbitals on the two atoms.

For example, in the case of  $\text{BaFe}_2\text{As}_2$ , we choose  $R = (0.5, 0, 0.25)$  and  $R' = (0.5, 0, -0.25)$ , and phases for all  $3d$  orbitals on the second atom are opposite to the first atom. For  $\text{LiFeAs}$  and  $\text{LaFeAsO}$ , we choose  $R = (0.75, 0.25, 0.5)$  and  $R' = (-0.75, -0.25, -0.5)$ , consequently the phase are opposite for  $\text{Fe-}d_{z^2}, d_{x^2-y^2}, d_{xy}$  and equal for  $d_{xz}$  and  $d_{yz}$  orbitals.

## B. Magnetic and Charge Susceptibility

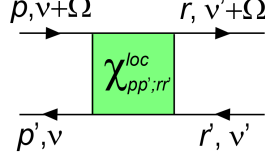


FIG. S1: Feynman diagram for the local two-particle susceptibility.

The general two-particle susceptibility (depicted in Fig.S1) is defined by

$$\chi_{pp';rr'}^{loc} = \langle \Psi_r^+(\tau_1) \Psi_{p'}^+(\tau_2) \Psi_{r'}(\tau_3) \Psi_p(\tau_4) \rangle \quad (\text{S2})$$

where  $p, p', r, r'$  are combined index of spin and orbital,  $\Psi^+$  is the creation operator and  $\Psi$  the annihilation operator.

The central quantity of this approach is the irreducible two particle vertex  $\Gamma$ , which consists of all Feynman diagrams, and can not be separated into two parts by cutting any two propagators. There are several types of irreducible vertices: i) the irreducible vertex in the particle-hole channel consists of all Feynman diagrams, which can not be separated into two parts by cutting any two propagators going in opposite direction, i.e., cutting a particle and a hole ii) the particle-particle irreducible vertex correspondingly contains diagrams which are not separated into parts by cutting any two propagators going in the same direction, iii) the fully irreducible two-particle vertex contains all diagrams which can not be broken into separate diagrams by cutting either particle-particle or particle-hole pair of propagators.

Within the Dynamical Mean Field Theory (DMFT), the particle-hole irreducible vertex  $\Gamma$  is local, and it is equal to the impurity vertex, which can be obtained from the solution of the quantum impurity model. This can be proven with the same power-counting arguments as the self-energy is proven to be local in the limit of large coordination number.[S1, S22] To compute  $\Gamma^{imp}$ , we sample the two-particle susceptibility  $\chi^{imp}$  by the quantum Monte Carlo impurity solver, and by inverting the Bethe-Salpeter equation, we obtain  $\Gamma^{imp}$ . For the the impurity model, the two-particle susceptibility is formally obtained by differentiating the partition function

$$\chi_{pp';rr'}^{imp} = \frac{1}{Z} \frac{\partial^2 Z}{\partial \Delta_{rp} \partial \Delta_{p'r'}} \quad (\text{S3})$$

and resulting terms are sampled by the quantum Monte Carlo solver. Notice that the susceptibility depends on four times, which can be translated into three frequencies. It turns out that this two-particle susceptibility can be broken up into two terms, of which both depend on two frequencies only, which greatly reduces the complexity of the problem. We sample these terms directly in frequency during the Monte Carlo run, just like the single-particle Green's function, to avoid the Fourier transform of a multidimensional object.

Once the impurity two-particle susceptibility  $\chi_{pp';rr'}^{imp}$  is available, we compute the impurity polarization (bubble)  $\chi_{pp'\nu;rr'\nu'}^{0,imp}$ , and extract the particle-hole irreducible vertex  $\Gamma_{pp'\nu;rr'\nu'}^{imp}$  by the Bethe-Salpeter equation:

$$\chi_{pp'\nu;rr'\nu'}^{imp} = \chi_{pp'\nu;rr'\nu'}^{0,imp} + \chi_{pp'\nu;p_1p'_1\nu_1}^{0,imp} \Gamma_{p_1p'_1\nu_1;r_1r'_1\nu'_1}^{imp} \chi_{r_1r'_1\nu'_1;rr'\nu'}^{imp} \quad (\text{S4})$$

as

$$\Gamma_{pp'\nu;rr'\nu'}^{imp} = (\chi_{pp'\nu;rr'\nu'}^{0,imp})^{-1} - (\chi_{pp'\nu;rr'\nu'}^{imp})^{-1} \quad (\text{S5})$$

where  $p, p', r, r'$  are combined index of spin and orbital, and  $\nu, \nu'$  are fermionic Matsubara frequencies. These equations depend also on the bosonic (center of mass) frequency  $\Omega$ , which can be treated as an external parameter.



With the knowledge of the particle-hole irreducible vertex, we can compute the non-local two particle susceptibility by the Bethe-Salpeter equation

$$\chi_{pp'\nu;rr'\nu'}^q = \chi_{pp'\nu;rr'\nu'}^{0,q} + \chi_{pp'\nu;p_1p'_1\nu_1}^{0,q} \Gamma_{p_1p'_1\nu_1;r_1r'_1\nu'_1}^{loc} \chi_{r_1r'_1\nu'_1;rr'\nu'}^q \quad (\text{S6})$$

as

$$\chi_{pp'\nu;rr'\nu'}^q = ((\chi^{0,q})^{-1} - \Gamma^{loc})_{pp'\nu;rr'\nu'}^{-1} \quad (\text{S7})$$

where  $\chi_{pp'\nu;rr'\nu'}^{0,q} = -T\delta(\nu - \nu') \sum_k G_{k,rp}(i\nu)G_{k-q,p'r'}(i\nu - i\Omega)$  is the nonlocal one-particle bubble. This ladder sum in the particle-hole channel incorporates most important non-local spin and orbital fluctuations.

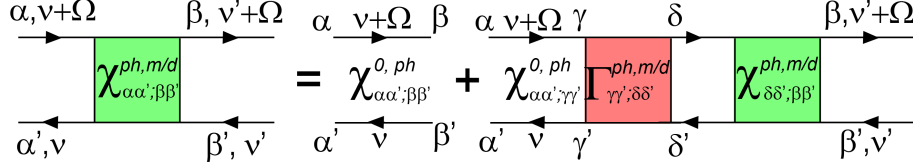


FIG. S2: **Feynman diagram for computing the local and momentum-dependent two-particle susceptibility in the particle-hole spin (m) and charge (d) channels.** Here the particle-hole irreducible vertex  $\Gamma$  is assumed to be local. The momentum-dependent two-particle susceptibility is obtained by using the momentum-dependent one-particle bubble  $\chi_q^0$ . The spin and charge susceptibility is computed by closing the corresponding two-particle susceptibility with the spin or charge bare vertex, and tracing over the internal indices, such as orbital ( $\alpha, \alpha', \beta, \beta'$ ) and frequency ( $\nu, \nu'$ ).

In the paramagnetic state (when the spin-orbit coupling is ignored), there is a symmetry between the states with different spin, and the equations can be block-diagonalized in spin. The following holds in paramagnetic state  $\chi_{\uparrow\uparrow;\uparrow\uparrow} = \chi_{\downarrow\downarrow;\downarrow\downarrow}$  and  $\chi_{\uparrow\uparrow;\downarrow\downarrow} = \chi_{\downarrow\downarrow;\uparrow\uparrow}$  where the orbital index is omitted for simplicity. As a result, the two-particle quantities can be expressed in terms of two independent channels (no mixing between the two channels), the magnetic and the charge channel as

$$\chi^m = \chi_{\uparrow\uparrow;\uparrow\uparrow} - \chi_{\uparrow\uparrow;\downarrow\downarrow} \quad (\text{S8})$$

$$\Gamma^m = \Gamma_{\uparrow\uparrow;\uparrow\uparrow} - \Gamma_{\uparrow\uparrow;\downarrow\downarrow} \quad (\text{S9})$$

$$\chi^d = \chi_{\uparrow\uparrow;\uparrow\uparrow} + \chi_{\uparrow\uparrow;\downarrow\downarrow} \quad (\text{S10})$$

$$\Gamma^d = \Gamma_{\uparrow\uparrow;\uparrow\uparrow} + \Gamma_{\uparrow\uparrow;\downarrow\downarrow} \quad (\text{S11})$$

Thus  $\chi_{\uparrow\uparrow;\uparrow\uparrow} = (\chi^d + \chi^m)/2$  and  $\chi_{\uparrow\uparrow;\downarrow\downarrow} = (\chi^d - \chi^m)/2$ . In addition, we have the following symmetry

$$\langle S^z(\tau)S^z(0) \rangle = \langle S^+(\tau)S^-(0) \rangle = \langle S^-(\tau)S^+(0) \rangle \quad (\text{S12})$$

Accordingly we have  $\chi_{\downarrow\uparrow;\downarrow\uparrow} = \chi_{\uparrow\downarrow;\uparrow\downarrow} = \chi^m$ . Hence the spin index can be dropped in the paramagnetic state by using the above vertex in the magnetic and charge channel. As shown in Fig.S2, the two-particle vertex in the magnetic/charge (m/d) channel can be written as

$$\chi_{\alpha\alpha';\beta\beta'}^{m/d}(\nu, \nu')_{q,\Omega} = ((\chi^0)_{q,\Omega}^{-1} - \Gamma^{m/d})_{\alpha\alpha';\beta\beta'}^{-1}(\nu, \nu')_{q,\Omega} \quad (\text{S13})$$

The spin or charge susceptibility  $\chi(q, \omega)$  is obtained by closing the corresponding nonlocal two-particle susceptibility  $\chi_{\alpha\alpha';\beta\beta'}^{m/d}(\nu, \nu')_{q,\Omega}$  with the bare vertex  $\mu$  and summation over the internal indices

$$\chi^{m/d}(q, \Omega) = 2 \sum_{\alpha, \alpha', \beta, \beta', \nu, \nu'} \mu_{\alpha\alpha'} \chi_{\alpha\alpha';\beta\beta'}^{m/d}(\nu, \nu')_{q,\Omega} \mu_{\beta\beta'} \quad (\text{S14})$$

Further computational details on magnetic susceptibility are available in Ref. S4.

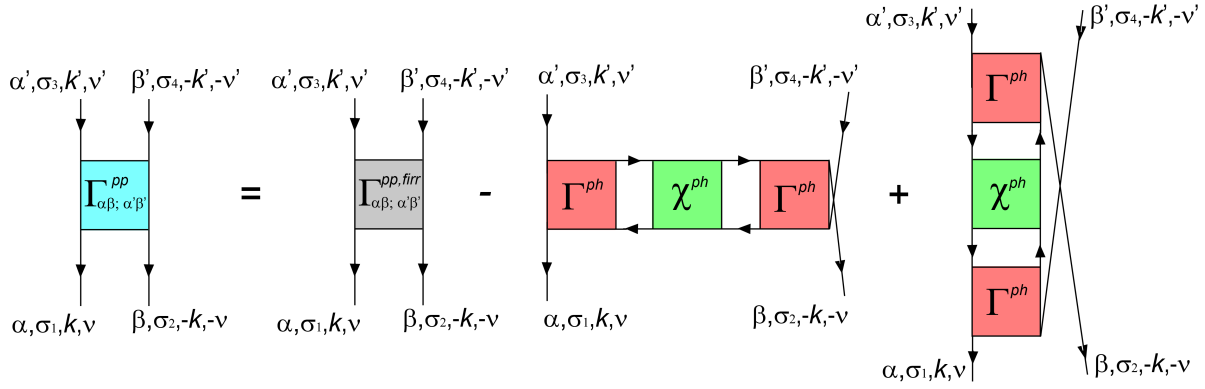


FIG. S3: **Particle-particle irreducible vertex**  $\Gamma_{\sigma_1\sigma_2;\sigma_3\sigma_4}^{pp}$ . It consists of fully-irreducible vertex  $\Gamma^{pp, f irr}$ , and vertex which is reducible in the particle-hole channel. There are two ways to arrange particle-hole ladders, either horizontally ( $\Gamma^{pp(1)}$ ) or vertically ( $\Gamma^{pp(2)}$ ), hence there are two particle-hole contributions.

### C. Superconductivity

A divergent susceptibility in the particle-particle channel signals instability of the metallic state towards superconductivity. To obtain this susceptibility, we need to compute the particle-particle irreducible vertex  $\Gamma^{pp}$ , depicted in Fig.S3. It consists of the fully irreducible vertex function  $\Gamma^{f irr}$  and the reducible vertex functions in the particle-hole channels. There are two particle-hole channels, because one can stack particle-hole ladders horizontally (particle-hole channel 1) or vertically (particle-hole channel 2), as shown in Fig.S3. Notice that this equation contain all spin-fluctuation diagrams [S23]. Indeed we recover the spin-fluctuation theory if we replace  $\Gamma^{ph}$  by constant number  $U$ , which is treated as a phenomenological parameter in spin-fluctuation theory, and propagators with free-electron Green's function. Since results are very sensitive to the value and structure of this screened interaction  $\Gamma^{ph}$ , it is important to determine it *ab initio*.

In this report, we consider only the spin-singlet pairing and define the singlet vertex  $\Gamma^{pp, s}$  by

$$\Gamma^{pp, s} = \frac{1}{2}(\Gamma_{\uparrow\downarrow; \uparrow\downarrow}^{pp} - \Gamma_{\uparrow\downarrow; \downarrow\uparrow}^{pp}) \quad (\text{S15})$$

For convenience, we rewrite  $\Gamma^{pp, s}$  as the sum of the three terms depicted in Fig. S4:

$$\Gamma^{pp, s} = \Gamma^{pp, f irr, s} + \Gamma^{pp(1), s} + \Gamma^{pp(2), s}. \quad (\text{S16})$$

It then follows that the fully irreducible particle-particle vertex in the spin singlet channel  $\Gamma^{pp, f irr, s}$  is

$$\Gamma^{pp, f irr, s} = \frac{1}{2}(\Gamma_{\uparrow\downarrow; \uparrow\downarrow}^{pp, f irr, s} - \Gamma_{\uparrow\downarrow; \downarrow\uparrow}^{pp, f irr, s}), \quad (\text{S17})$$

We can also express the rest of the objects in Fig. S4 in terms of the above calculated particle-hole susceptibility  $\chi^{ph}$  and particle-hole irreducible vertex  $\Gamma^{ph}$  by

$$\begin{aligned} \Gamma^{pp(1), s} &= -\frac{1}{2}((\Gamma\chi\Gamma)_{\uparrow\uparrow; \downarrow\downarrow}^{ph} - (\Gamma\chi\Gamma)_{\downarrow\uparrow; \downarrow\uparrow}^{ph}) \\ &= \frac{3}{4}(\Gamma\chi\Gamma)^{ph, m} - \frac{1}{4}(\Gamma\chi\Gamma)^{ph, d} \end{aligned} \quad (\text{S18})$$

and

$$\begin{aligned} \Gamma^{pp(2), s} &= \frac{1}{2}((\Gamma\chi\Gamma)_{\downarrow\uparrow; \downarrow\uparrow}^{ph} - (\Gamma\chi\Gamma)_{\uparrow\uparrow; \downarrow\downarrow}^{ph}) \\ &= \frac{3}{4}(\Gamma\chi\Gamma)^{ph, m} - \frac{1}{4}(\Gamma\chi\Gamma)^{ph, d} \end{aligned} \quad (\text{S19})$$

These diagrams are depicted in Fig. S4.

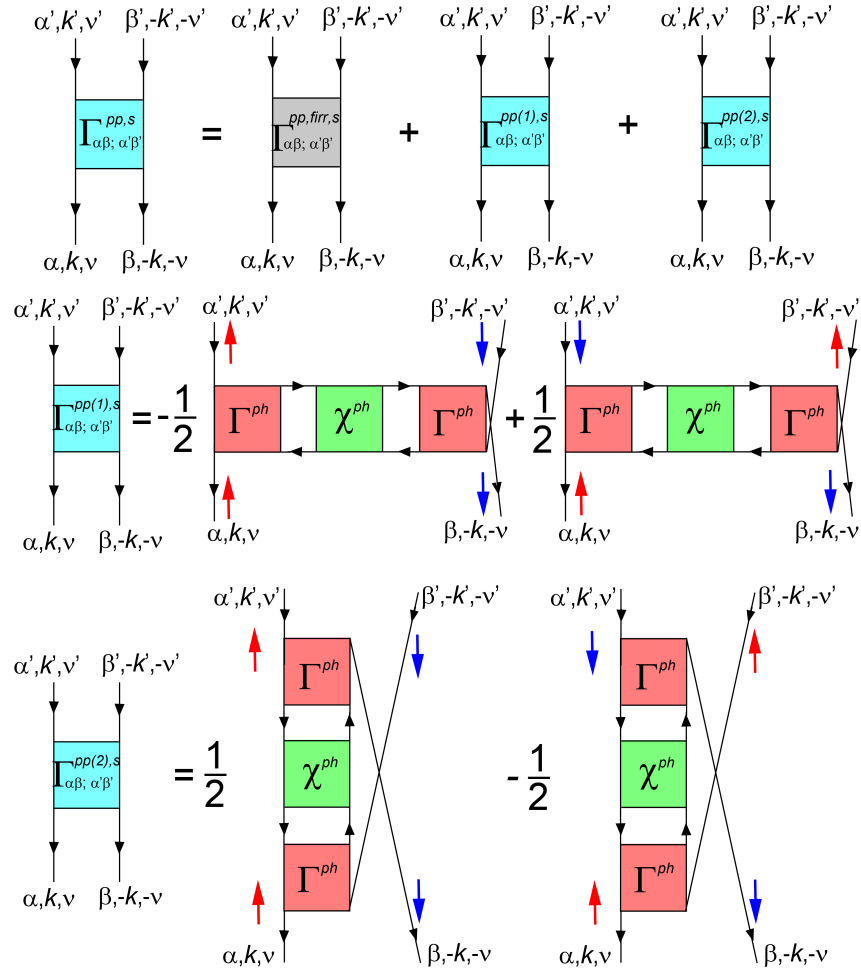


FIG. S4: **Decomposition of particle-particle irreducible vertex for the spin singlet channel:** We explicitly write the spin components, which contribute to the vertex  $\Gamma^{pp,s}$  in the singlet channel.

To simplify the notation, we then define

$$(\overline{\Gamma\chi\Gamma})^{ph} \equiv \frac{3}{4}(\Gamma\chi\Gamma)^{ph,m} - \frac{1}{4}(\Gamma\chi\Gamma)^{ph,d}. \quad (\text{S20})$$

to connect the above computed magnetic and charge susceptibility/vertex with the particle-particle irreducible vertex. With this algebraic manipulation, we removed the need for the spin index, however, we do have four orbital indices ( $\alpha, \beta, \alpha', \beta'$ ), three frequencies (fermionic  $\nu, \nu'$ , and bosonic  $\Omega$ ) and three momenta ( $k, k', q$ ) left. However, within DMFT the particle-hole irreducible vertex  $\Gamma^{ph}$  is local, therefore this quantity is independent of momenta  $k$  and  $k'$  and can be written as

$$(\overline{\Gamma\chi\Gamma})_{q,\Omega}^{ph}(\alpha\beta, \nu; \alpha'\beta', \nu') \quad (\text{S21})$$

Furthermore, the fully irreducible vertex within DMFT is local and hence independent of momenta  $\Gamma_{\alpha\beta\nu; \alpha'\beta'\nu'}^{pp,irr,s}(\alpha\beta\nu; \alpha'\beta'\nu')$ .

Finally, using these building blocks computed above, we explicitly write down the irreducible particle-particle vertex

$$\begin{aligned} \Gamma^{pp,s}(\alpha\beta k\nu; \alpha'\beta' k'\nu') &= \Gamma^{pp(1),s}(\alpha\beta k\nu; \alpha'\beta' k'\nu') + \Gamma^{pp(2),s}(\alpha\beta k\nu; \alpha'\beta' k'\nu') + \Gamma^{pp,irr,s}(\alpha\beta\nu; \alpha'\beta'\nu') \\ &= (\overline{\Gamma\chi\Gamma})_{k'-k, \nu'-\nu}^{ph}(\alpha'\alpha, \nu'; \beta\beta', -\nu) + (\overline{\Gamma\chi\Gamma})_{-k'-k, -\nu'-\nu}^{ph}(\beta'\alpha, -\nu'; \beta\alpha', -\nu) + \Gamma^{pp,irr,s}(\alpha\beta\nu; \alpha'\beta'\nu') \end{aligned} \quad (\text{S22})$$

When the particle-particle ladder sum  $\chi^{pp} = ((\chi^{0,pp})^{-1} - \Gamma^{pp})^{-1}$  is diverging, the normal state is unstable to superconductivity. The sufficient condition is that the matrix of  $\Gamma^{pp}\chi^{0,pp}$  has an eigenvalue equal to unity. The eigenvector

with the largest eigenvalue gives the symmetry of the superconducting order parameter. Explicitly, we are solving the eigenvalue problem of the following matrix

$$-k_B T \sum_{k'\nu'\alpha'\beta'\gamma\delta} \Gamma^{pp,s}(\alpha\beta k\nu; \alpha'\beta'k'\nu') \chi_{\alpha'\beta'\gamma\delta}^{0,pp}(k'\nu') \Delta_{\gamma\delta}(k'\nu') = \lambda \Delta_{\alpha\beta}(k\nu) \quad (\text{S23})$$

where the eigenvalue  $\lambda$  is the pairing strength and the eigenfunction  $\Delta$  is the pairing amplitude.

To solve this eigenvalue problem, we make an approximation consistent with the Bardeen-Cooper-Schrieffer (BCS) theory: since pairing occurs at very low energy scale, we take the particle-particle vertex at zero frequency as a proxy for its steep rise with lowering temperature, i.e.,  $\Gamma^{pp,s}(\alpha\beta k, \nu; \alpha'\beta'k', \nu') \approx \Gamma^{pp,s}(\alpha\beta k, 0^+; \alpha'\beta'k', 0^+)$ , hence we have

$$- \sum_{k'\alpha'\beta'\gamma\delta} \Gamma^{pp,s}(\alpha\beta k 0^+; \alpha'\beta'k' 0^+) \left( k_B T \sum_{i\nu'} \chi_{\alpha'\beta'\gamma\delta}^{0,pp}(k', \nu') \right) \Delta_{\gamma\delta}(k' 0^+) = \lambda \Delta_{\alpha\beta}(k 0^+) \quad (\text{S24})$$

where  $k_B T \sum_{\nu'} \chi_{\alpha'\beta'\gamma\delta}^{0,pp}(k', \nu') = k_B T \sum_{\nu'} G_{\alpha'\gamma}(k', \nu') G_{\beta'\delta}(-k', -\nu')$  is the one-particle bubble in the particle-particle channel.

To facilitate this calculation, we first transform the single-particle Green's function to one-iron atom Brillouin zone. We then compute pairing strength in orbital basis  $\Delta_{\alpha\beta}(k)$  with above formula, and we finally transform it to quasiparticle band basis by so-called embedding method. For DMFT calculation, we construct projector to iron-3d states  $U_k$  (for details see Ref. S2), which embeds the self-energy to the Kohn-Sham basis ( $U_k \Sigma U_k^\dagger$ ) or projects Green's function expressed in the Kohn-Sham basis to local basis ( $U_k^\dagger G U_k$ ). We then compute the eigenvectors and eigenvalues of the DMFT Green's function at the Fermi level, defined by

$$(\varepsilon_k - \mu + U_k \Sigma(\omega = 0) U_k^\dagger) \psi^R(k) = \epsilon_k \psi^R(k) \quad (\text{S25})$$

$$\psi^L(k) (\varepsilon_k - \mu + U_k \Sigma(\omega = 0) U_k^\dagger) = \epsilon_k \psi^L(k) \quad (\text{S26})$$

where  $\epsilon_k$  are the DMFT eigenvalues at the Fermi level, which determine the Fermi surface, and  $\psi(k)$  are the eigenvectors. We can then express the pairing strength on the Fermi surface as

$$\Delta_k \equiv \psi_k^L U_k \Delta(k) U_k^\dagger \psi_k^R \quad (\text{S27})$$

Notice that  $\Delta_k$  contains both the diagonal and off-diagonal components in band basis. The latter are smaller, hence we plot diagonal components in the manuscript  $\Delta_{k,ii}$ .

---

\* Electronic address: yinzping@physics.rutgers.edu

- [S1] Kotliar, G., Savrasov, S. Y., Haule, K., Oudovenko, V. S., Parcollet, O. & Marianetti, C. A. Electronic structure calculations with dynamical mean-field theory. *Rev. Mod. Phys.* **78**, 865-951 (2006).
- [S2] Haule, K., Yee, C.-H. & Kim, K. Dynamical mean-field theory within the full-potential methods: electronic structure of CeIrIn<sub>5</sub>, CeCoIn<sub>5</sub>, and CeRhIn<sub>5</sub>. *Phys. Rev. B* **81**, 195107 (2010).
- [S3] Blaha, P., Schwarz, K., Madsen, G. K. H., Kvasnicka, D. & Luitz, J. WIEN2K An augmented plane wave + local orbitals program for calculating crystal properties, (K. Schwarz, Techn. Univ. Wien, Austria, 2001).
- [S4] Park, H., Haule, K., & Kotliar, G. Magnetic Excitation Spectra in BaFe<sub>2</sub>As<sub>2</sub>: A Two-Particle Approach within a Combination of the Density Functional Theory and the Dynamical Mean-Field Theory Method. *Phys. Rev. Lett.* **107**, 137007 (2011).
- [S5] Haule, K. Quantum Monte Carlo impurity solver for cluster dynamical mean-field theory and electronic structure calculations with adjustable cluster base. *Phys. Rev. B* **75**, 155113 (2007).
- [S6] Werner, P., Comanac, A., de Medici, L., Troyer, M. & Millis, A. J. Continuous-time solver for quantum impurity models. *Phys. Rev. Lett.* **97**, 076405 (2006).
- [S7] Yin, Z.P., Haule, K., & Kotliar, G. Kinetic frustration and the nature of the magnetic and paramagnetic states in iron pnictides and iron chalcogenides. *Nature Materials* **10**, 932-935 (2011).
- [S8] Tropeano, M., Pallecchi, I., Cimberle, M. R., Ferdeghini, C., Lamura, G., Vignolo, A., Martinelli, A., Palenzona, A. & Putti, M. Transport and superconducting properties of Fe-based superconductors: SmFeAs(O<sub>1-x</sub>F<sub>x</sub>) versus Fe<sub>1+y</sub>(Te<sub>1-x</sub>Se<sub>x</sub>). *Supercond. Sci. Technol.* **23**, 054001 (2010).
- [S9] Martinelli, A., Palenzona, A., Tropeano, M., Ferdeghini, C., Putti, M., Cimberle, M. R., Nguyen, T. D., Affronte, A. & Ritter, C. From antiferromagnetism to superconductivity in Fe<sub>1+y</sub>(Te<sub>1-x</sub>Se<sub>x</sub>) (0 < x < 0.20): a neutron powder diffraction analysis. *Phys. Rev. B* **81**, 094115 (2010).
- [S10] Guo, J. G., Jin, S. F., Wang, G., Wang, S. C., Zhu, K. X., Zhou, T. T., He, M. & Chen, X. L. Superconductivity in the iron selenide K<sub>x</sub>Fe<sub>2</sub>Se<sub>2</sub> (0 ≤ x ≤ 1.0). *Phys. Rev. B* **82**, 180520(R) (2010).

- [S11] Phelan, D., Millican, J. N., Thomas, E. L., Leao, J. B., Qiu, Y. & Paul, P. Neutron scattering Measurements of the phonon density of states of  $\text{FeSe}_{1-x}$  superconductors. *Phys. Rev. B* **79**, 014519 (2009).
- [S12] Tapp, J. H., Tang, Z. J., Lv, B., Sasmal, K., Lorenz, B., Chu, P. C. W. & M. Guloy, A. M.  $\text{LiFeAs}$ : an intrinsic FeAs-based superconductor with  $T_c = 18\text{K}$ . *Phys. Rev. B* **78**, 060505(R) (2008).
- [S13] Johrendt, D. & Poettgen, R. Superconductivity, magnetism and crystal chemistry of  $\text{Ba}_{1-x}\text{K}_x\text{Fe}_2\text{As}_2$ . *Physica C* **469**, 332-339 (2009).
- [S14] Rotter, M., Tegel, M., Johrendt, D., Schellenberg, I., Hermes, W., & Pöttgen, R. Spin-density-wave anomaly at 140 K in the ternary iron arsenide  $\text{BaFe}_2\text{As}_2$ . *Phys. Rev. B* **78**, 020503(R) (2008).
- [S15] Kamihara, Y., Watanabe, T., Hirano, M. & Hosono, H. Iron-based layered superconductor  $\text{La}[\text{O}_{1-x}\text{F}_x]\text{FeAs}$  ( $x = 0.05-0.12$ ) with  $T_c = 26\text{K}$ . *J. Amer. Chem. Soc.* **130**, 3296-3297 (2008).
- [S16] Tegel, M., Rotter, M., Weiss, V., Schappacher, F. M., Poettgen, R. & Johrendt, D. Structural and magnetic phase transitions in the ternary iron arsenides  $\text{SrFe}_2\text{As}_2$  and  $\text{EuFe}_2\text{As}_2$ . *J. Phys.: Condens. Matter* **20**, 452201 (2008).
- [S17] Kamihara, Y., Hiramatsu, H., Hirano, M., Kawamura, R., Yanagi, H., Kamiya, T. & Hosono, H. Iron-based layered superconductor:  $\text{LaOFeP}$ . *J. Am. Chem. Soc.* **128**, 10012-10013 (2006).
- [S18] Deng, Z., Wang, X.C., Liu, Q.Q., Zhang, S.J., Lv, Y.X., Zhu, J.L., Yu, R.C., & Jin, C.Q. A new 111 type iron pnictide superconductor  $\text{LiFeP}$ . *Europhys. Lett.* **87**, 3704 (2009).
- [S19] Analytis, J.G., Chi, J.-H., McDonald, R.D., Riggs, S.C., & Fisher, I.R. Enhanced Fermi surface nesting in superconducting  $\text{BaFe}_2(\text{As}_{1-x}\text{P}_x)_2$  revealed by de Haas-van Alphen effect. *Phys. Rev. Lett.* **105**, 207004 (2010).
- [S20] Kutepov, A., Haule, K., Savrasov, S. Y. & Kotliar, G. Self consistent GW determination of the interaction strength: application to the iron arsenide superconductors. *Phys. Rev. B* **82**, 045105 (2010).
- [S21] Yin, Z. P., Haule, K. & Kotliar, G. Magnetism and charge dynamics in iron pnictides. *Nat. Phys.* **7**, 294-297 (2011).
- [S22] Georges, A., Kotliar, G., Krauth, W., & Rozenberg, M.J. Dynamical mean-field theory of strongly correlated fermion systems and the limit of infinite dimensions. *Rev. Mod. Phys.* **68**, 13-125 (1996).
- [S23] Hirschfeld, P.J., Korshunov, M.M., & Mazin, I.I. Gap symmetry and structure of Fe-based superconductors. *Rep. Prog. Phys.* **74**, 124508 (2011).